Journal of Natural Gas Science and Engineering 43 (2017) 69–80

Contents lists available at ScienceDirect

Journal of Natural Gas Science and Engineering

journal homepage: www.elsevier.com/locate/jngse

Natural fractures initiation and fracture type prediction in coal reservoir under different *in-situ* stresses during hydraulic fracturing

Saipeng Huang [a], Dameng Liu [a], Yanbin Yao [a], Quan Gan [b], Yidong Cai [a, *], Lulu Xu [a]

[a] Coal Reservoir Laboratory of National Engineering Research Center of CBM Development & Utilization, School of Energy Resources, China University of Geosciences, Beijing, 100083, China
[b] School of Geosciences, King's College, University of Aberdeen, AB24 3UE, Aberdeen, UK

ARTICLE INFO

Article history:
Received 2 September 2016
Received in revised form
14 March 2017
Accepted 17 March 2017
Available online 4 April 2017

Keywords:
Natural fracture initiation
Finite element method
Lateral stress coefficient
Hydraulic fracturing

ABSTRACT

Hydraulic fracturing is one of the most effective ways of formation stimulation for enhancing coalbed methane (CBM) recovery. The fracture initiation and propagation during hydraulic fracturing is primary constrained by local stress field, hydraulic pressure magnitude, coal properties, and natural fractures. In this work, the fracture initiation region and propagation direction during hydraulic fracturing under various *in-situ* stresses were investigated both experimentally and numerically. For experimental study, fracturing under true tri-axial stresses was designed to determine the fracture propagation under two sets of *in-situ* stresses. And for numerical study, a single-fracture model was constructed by using finite element method (FEM3D) ANSYS workbench, which indicates that high lateral stress coefficient is conducive to create new compressive fractures instead of shear fractures. $\sigma_H = \sigma_v$ or $\sigma_h = \sigma_v$ has a great influence on the initiation location that determined by θ (from -90° to 90°) of the compressive fracture, while there is no significant influence on shear fracture. With the same σ_v applied, the horizontal stress difference has slightly impact on the type of newly-created fracture. The value of lateral stress coefficient that ranges from 0.35 to 1.20 decides the fracture type, which plays a crucial role in determining the stress magnitude and orientation around the fracture tip. The horizontal and vertical fracture are the main types when $\sigma_v > \sigma_H > \sigma_h$ and $\sigma_H > \sigma_v > \sigma_h$ respectively. The inclined fractures are possibly created in the coals with strong heterogeneity. Therefore, they can be used to predict the direction of initiation and propagation for the type of newly-created fracture during hydraulic fracturing for coalbed methane (CBM) development.

1. Introduction

Hydraulic fracturing is an effective method to improve the permeability of hydrocarbon reservoirs, which has been widely used in the exploitation of unconventional gases (e.g. shale gas and coalbed methane (CBM)) (Zhang and Chen, 2010; Majdi et al., 2012; Huang et al., 2013; Wang et al., 2014). The natural fractures (also called cleats in coal) properties, including cleat morphology, density and aperture, and matrix-cleat interaction examined through cleat surfaces, are essential for planning CBM exploration and production (Karacan and Okandan, 2000). The permeability of coal, especially for the high rank coals (normally<0.5 mD), is very low even with well-developed natural fractures due to bad connectivity between fractures (Cai et al., 2011). Therefore, hydraulic fracturing is wide applied for CBM commercial production, which creates new hydraulic fractures and improves the connectivity of pre-existing natural fractures. The impact of local stress distribution on the direction and development of newly-created fractures has been investigated extensively by Jaeger and Cook (1979), Hickman et al. (1985), Charlez and Despax (1985), Brudy and Zoback (1999), Nelson (2005), Ameen (2014). The natural fractures initiation during fracturing is critical for CBM production, whereas the understanding of initiation mechanism of natural fractures is still unclear. Orientation of fractures and horizontal principal stresses were compared (Brudy and Zoback, 1999), which demonstrated that the fractures orientation could be the reliable indicators for the orientation of the maximum horizontal principal stress. Previously, Li et al. (2014) has confirmed that horizontal differential stress is one of the dominating factors for the initiation of hydraulic fractures, whereas the effects of the existed fractures' geometry, tensile/shear

* Corresponding author.
E-mail address: yidong.cai@cugb.edu.cn (Y. Cai).

http://dx.doi.org/10.1016/j.jngse.2017.03.022
1875-5100/

strength, anisotropy and temperature of rock, and the magnitude of the hydraulic pressure (Heffer and Koutsabeloulis, 1995; Laubach et al., 2004; Philip et al., 2005; Taleghani and Olson, 2011) on the fracture initiation have not yet been clearly revealed. An extended finite element method model was ever adopted (Taleghani and Olson, 2014) to demonstrate the sensitivity of the fracture geometry on differential stress, natural fracture orientation, and the *in-situ* maximum compressive stress. The relation between semi-log of fracture closure and stress proved that natural fracture closure is very sensitive to the effective horizontal stress ratio (Hillis, 1998). Recently, natural fracture propagation mechanisms have aroused the interests of multiple researchers (Gordeliy and Peirce, 2013; Rahman and Rahman, 2013; Li et al., 2014; Zhai et al., 2015). Zhou et al. (2008) found that shear strength of natural fracture should be one of the factors influencing fracture propagation. However, the experimental results by Liu et al. (2014) agreed that the principle of hydraulic fracture propagation follows the least resistance and the shortest propagation path. After that, Stoeckhert et al. (2015) found that tensile fracturing in anisotropic rocks could result in complex fracture geometries. The previous work also indicated that the propagation of hydraulic fracture is commonly influenced by engineering parameters such as the type, viscosity and injection flow rate of fracturing fluid (Bohloli and Pater, 2006; Shimizu et al., 2011; Guo et al., 2014). Fracturing experiments carried out by Bohloli and Pater (2006) indicated that fluid rheology has a strong influence on fracturing behavior, and they found that fracturing fluid with cross-linked gel with quartz powder is one of the most effective fluids to create new fractures.

At the same time, a number of numerical simulation research (Moes et al., 1999; Beekman et al., 2000; Li and Wong, 2012; Yao, 2012; Kim and Moridis, 2015) about the fracturing process and propagation of newly-created fractures have been carried out. For examples, a 2D model developed by Cleary and Wong (1985) allowed detail tracing of pressure distribution and fluid flow in the fracture, which was used in a fully 3D hydro-frac simulator. Jeffrey et al. (2009) performed numerical simulation of hydraulic fracturing process using a 3D planar hydraulic fracture model, and the simulated results were consistent with that from experimental. Apart from that, the arbitrary tetrahedral meshes (Paluszny and Zimmerman, 2011) were used in numerical simulation for 3D propagating fractures, which shows very limited deviation. The fracture breakout angle and breakout depth, as important factors for fracturing initiation, show an excellent consistency with the observations in laboratory, if the fracture initiation strength is fixed (Rinne et al., 2013). A 2D double-fracture model was established by Silva and Einstein (2014), of which the ratio between water pressure and vertical load plays a crucial role in the stress field around a fracture tip. Therefore it may affect the location of tensile and generation of shear fracture. Recently, Mcclure et al. (2016) revealed that the orientation of original fractures and stress anisotropy should be the main factors to influence the propagation of hydraulic fracture, especially when the propagating hydraulic fracture encounters natural fracture. Moreover, a similar numerical simulation study carried out by Wasantha et al. (2017) further indicated that the hydraulic fractures initiate on the side having a weak natural fracture (i.e. the stiffness of natural fractures is lower) more efficiently grow towards it while the fracture propagation in the opposite direction is merely stopped, which manifest that the zone with lower stiffness in the reservoir is beneficial to hydraulic fracturing and improve reservoir permeability. Furthermore, numerical simulation by Wang et al. (2014) showed the fracture radius is mainly influenced by the mechanics parameters such as elasticity modulus and Poisson's ratio.

Previous works (Zhou et al., 2008; Rinne et al., 2013; Stoeckhert et al., 2015) focused on the impacts of rock mechanics and complex natural fracture system on fracture initiation and propagation. Although the horizontal stresses or vertical stress in 2D (Paul and Chatterjee, 2011; Silva and Einstein, 2013, 2014) has been considered to investigate the fracture direction, a few works (Chatterjee, 2008; Paluszny and Zimmerman, 2011) considered vertical stress and horizontal stresses in a 3D *in-situ* situation. Therefore, the mechanism of fracture initiation has not yet been well investigated and fully explained in a 3D stress field. This study aims to investigate the following unfathomed mechanism: 1) the effect of lateral stress coefficient on natural fracture initiation; 2) the relation between fracture initiation type and *in-situ* stresses. In the light of above targets, the geometry with single-fracture was created in ANSYS workbench under different maximum and minimum horizontal stresses, constant vertical stress and hydraulic pressures. The fracture initiation and type related to the magnitude and orientation of the maximum principle stress and maximum shear stress was also investigated. Furthermore, the experiments of hydraulic fracturing were conducted in a true tri-axial circumstance that referred to the *in-situ* stresses condition. And the hydraulic fracture created by the tri-axial experiments was detailed elucidated and compared with the fracturing results of the numerical simulation.

2. Experiments and methodology

2.1. Experimental simulation of hydraulic fracturing

A true tri-axial hydro-fracturing experiment is conducted on the coal block with a size of 300 mm*300 mm*300 mm. The true tri-axial pressure system is consist by a hydraulically voltage stabilizer, true tri-axial rig, isolating rigs of fracturing fluid and power oil, servo-supercharger, servo hydraulic pump and data acquisition system (Fig. 1). Firstly, the cubic sample is positioned in true tri-axial rig, and the pressure platens are equipped with spherical sheets to ensure equal pressure distribution. Then, the tri-axial stresses are provided by the servo hydraulic pump. The servo-supercharger and isolating rigs are used to inject the fracturing fluids (pure water with color tracer) into the sealed simulated wellbore (vertically) by the oil pressure. Finally, a data acquisition system automatically records the experimental data including flow rates of fracturing fluids, flow time and injection pressures. According to the principle of similarity criterion (Liu et al., 2000), the laboratory injection flow rates were both designed as $0.33/ml \cdot s^{-1}$, which is used to model the *in-situ* injection flow rate of $6.0/m^3 \cdot min^{-1}$. Although the results obtained by Bohloli and Pater (2006) proved that the pure water as fracturing fluid is not preferential, the pure water is still economic desirable in the field practice of Qinshui Basin, China. Therefore the pure water was used to comfort with this fracturing experiment.

The high-rank coal samples were collected from the No. 3 coal seam of the Shanxi Formation in the Zhengzhuang CBM field of Southern Qinshui Basin (SQB), North China (Figs. 2 and 3). The No. 3 coal seam with thicknesses of 3–7 m is one of the most continuous and stable coal seams of the SQB, which has relative stable coal structure and high gas content. And therefore it is currently the target seam for CBM development in the Southern Qinshui Basin, North China (Cai et al., 2011; Teng et al., 2015). The petrophysical properties of the selected coals are displayed in Table 1, which include compressive strength, Young's modulus, tensile strength and Poison's ratio. The values of vertical stress (σ_v) were set in the light of the *in-situ* depth of the selected coals in the Zhengzhuang area, and the values of maximum horizontal stress (σ_H) and minimum horizontal stress (σ_h) were set based on Kaiser effect (Kaiser, 1953; Li and Nordlund, 1993; Barr and Hunt, 1999; Filimonov et al., 2001; Lavrov, 2001; Lehtonen et al., 2012) tested on the coal blocks. The acquired values of tri-axial stresses ($\sigma_v/\sigma_H/\sigma_h$) of these two coal

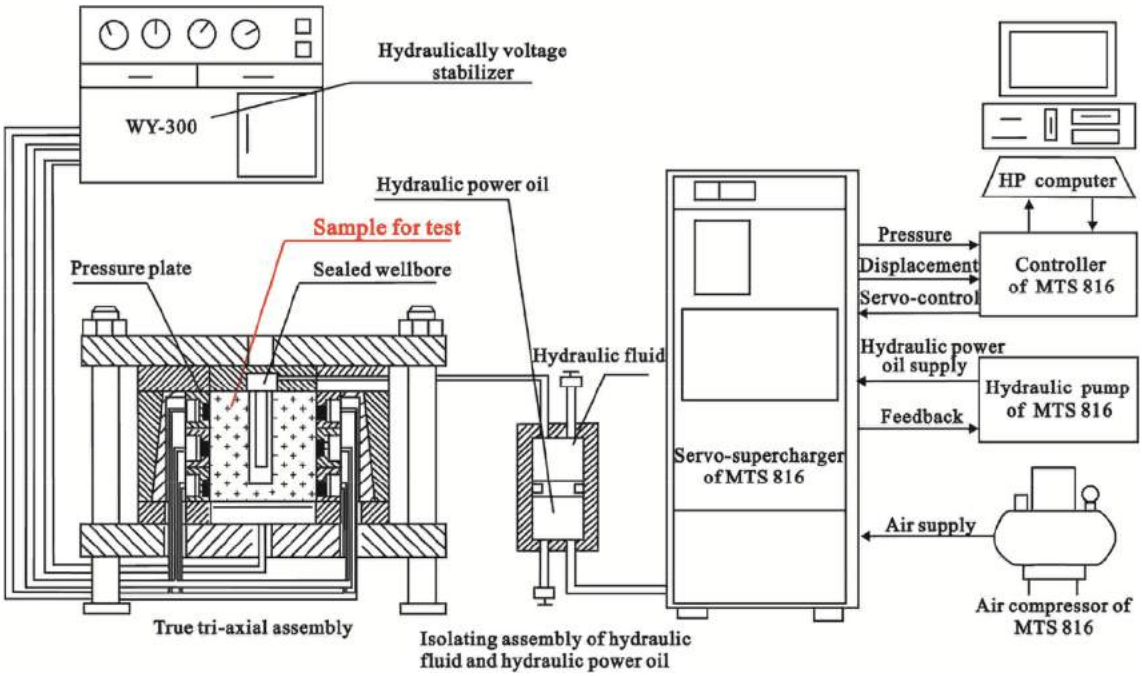

Fig. 1. The schematic of true tri-axial hydraulic fracturing experimental apparatus (Zhou et al., 2008).

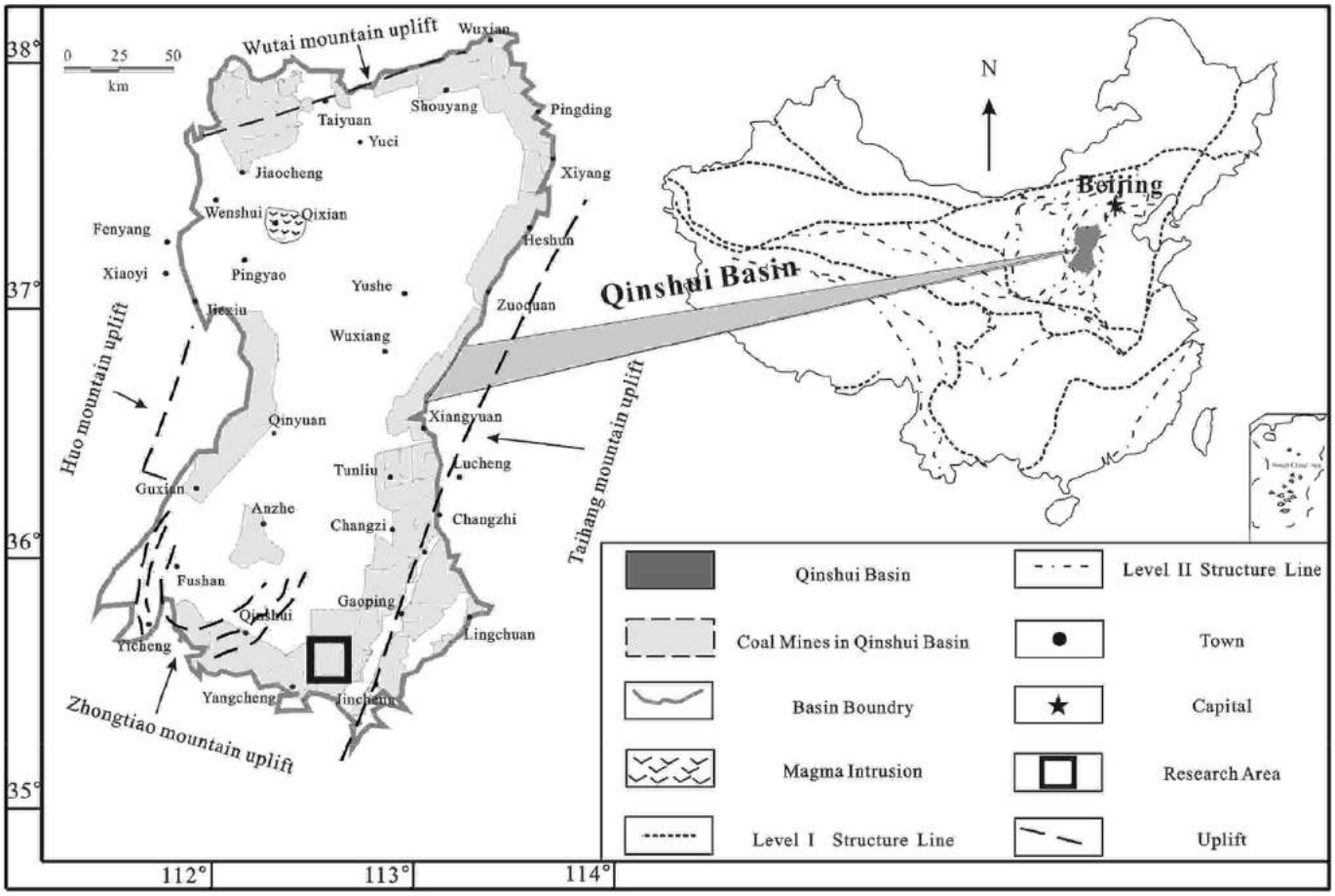

Fig. 2. The location map of the coalfields and the SQB in north China (Cai et al., 2011).

blocks were 17.6/17.3/11.3 MPa (sample 1#) and 18.2/20.4/16.4 MPa (sample 2#), respectively. These values of the σ_v, σ_H and σ_h will be adopted to simulate the natural fracture initiation at the *in-situ* stresses condition.

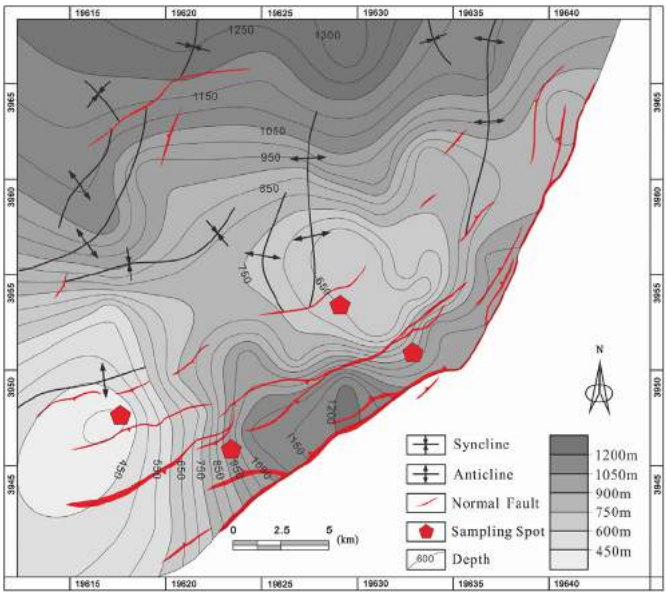

Fig. 3. Map of the research area showing the major structures and sampling spots in the SQB.

Table 1
The depth (D), density (DEN), compressive strength (σ_{bc}), Young's modulus (E), Poison's ratio (μ), tensile strength (σ_b) of totally 12 coal samples from 4 CBM exploration wells.

D (m)	DEN (g/cm^3)	σ_{bc} (MPa)	E (GPa)	μ	σ_b (MPa)
420	1.35–1.36	39.11–58.45	3.28–3.87	0.34–0.37	0.95–1.57
650	1.35–1.36	46.52–69.60	3.67–3.83	0.35–0.38	0.32–0.51
900	1.36–1.39	56.99–78.69	3.81–4.06	0.33–0.39	0.91–1.48
930	1.35–1.37	56.74–60.54	3.81–4.06	0.39–0.41	0.60–0.87

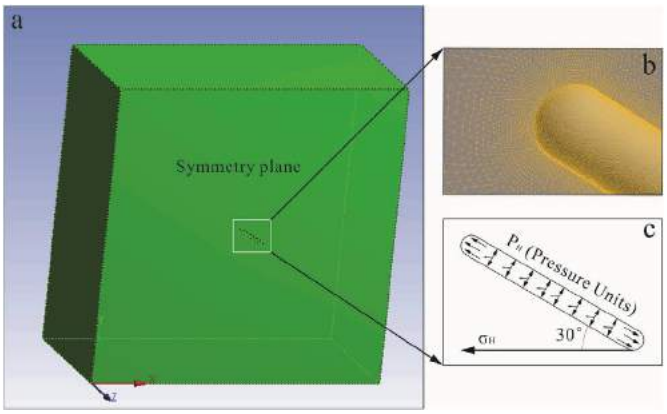

Fig. 4. Loading condition of the single-fracture model, (a) stress loading schematic, (b) the Finite Element mesh of the fracture tip, (c) P_H applied in the fracture. P_H stands for hydraulic pressure and 30° is the approaching angle between natural fracture and the direction maximum horizontal stress.

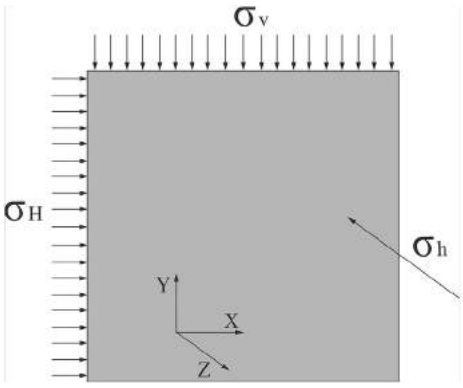

Fig. 5. The schematic of the element stress condition.

2.2. The numerical simulation

The numerical analysis was completed using the Finite Element Software of ANSYS workbench (Chatterjee, 2008; Paul and Chatterjee, 2011). To reduce the computing time, the symmetry analysis function in ANSYS workbench was employed in the symmetry plane (Fig. 4a). The fine mesh was used near the natural fracture where the stresses concentrated (Fig. 4b). Four loading modes including hydraulic pressure (P_H), σ_v, σ_H and σ_h were adopted in the numerical analysis. Initial hydraulic pressure ($P_H = 6$ MPa) was applied along the surface of the natural fracture, and the approaching angle between natural fracture and the direction maximum horizontal stress was set to be 30° (Fig. 4c).

The boundary conditions in the model are defined as shown in Fig. 5. All loadings were applied on the surfaces of the model. Displacement in each element was constrained along the directions of y-axis, z-axis, and x-axis, respectively. Hereby, the coal blocks was considered to be linearly elastic according to Silva and Einstein (2014), Therefore the finite element analysis was valid before initiating any fractures. In this paper, the Young's modulus, E, and Poison's ratio, μ, were given as 3.72 GPa and 0.37 respectively, more detailed is shown in Table 1.

The fracture tip is critical to determine stress distribution (Silva and Einstein, 2014). Thus, it is essential to choose a proper shape of the fracture tip. When the fracture tip presents in an irregular shape (e.g. the shape with sharp corners), the corresponded non-uniform mesh will lead to an abnormal stress distribution around the fracture tip without physical meaning. The meshing near the spherical shape of fracture tip is more uniform than any other shapes. For example, other stress paths around the flaw tip were ever studied by Silva and Einstein (2013), of which the differences in stresses between paths do not significantly affect the fracture initiation. Therefore, the fracture tip was set as hemispherical (Fig. 6a). Furthermore, due to the impact of stress and strain, a plastic zone may occur around the fracture edge without proper physical explanation. Under the above considerations, Silva and Einstein (2014) defined a stress path that is circled with double radius of the fracture tip, which was adopted in this study. The path varies along the semicircle with a θ ranging from −90° to 90° in anticlockwise (Fig. 6b). To conveniently extract data, the stress path is located on the symmetry plane (Fig. 4a).

2.2.1. Loading design of numerical simulation

The lateral stress coefficient (κ) that reflects the relation between horizontal stresses and the vertical stress (Hoek and Brown, 1980), commonly defined as $(\sigma_H+\sigma_h)/2\sigma_v$, is a critical parameter for simulating fracture initiation at the *in-situ* stresses condition. The previous work by Meng et al. (2011) showed that the measured results indicates that the lateral stress coefficients range generally from 0.42 to 1.42 with an average value of 0.82 in the Southern Qinshui Basin. In this study, the κ was estimated based on the actual burial depth of No. 3 coal seam in the Zhengzhuang field. Brown and Hoek (1978) provided a regression correlation between κ and the burial depth of a target seam:

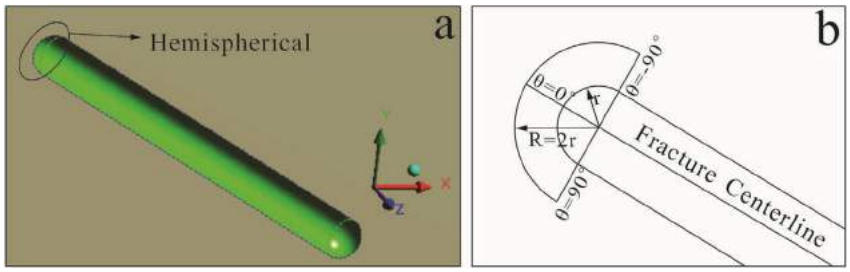

Fig. 6. (a) The shape of fracture tip, (b) Schematic of stress path, the θ range from −90° to 90°, and the relationship between the radius of fracture tip (r) and the radius of stress path (R) is R = 2r.

$$\frac{100}{d}+0.3\le\kappa\le\frac{1500}{d}+0.5 \quad (1)$$

where d is the burial depth in meters. The burial depth of the No.3 coal seam ranges from 300 m to 1300 m. Therefore, the κ values in this study are commonly of 0.35–1.20.

Fig. 7 shows that 13 total loading scenarios were executed in the numerical simulation. For each loading, the P_H and σ_v were kept constant as 6 MPa and 20 MPa, respectively. And the values of σ_H and σ_h vary from 6 MPa to 24 MPa. The actual values used in the simulation refer to the *in-situ* stress distribution of the research area.

2.2.2. Definition of stress state of elements

A 3D Mohr circle was provided to analyze the stress condition through the finite elements of the numerical simulation. For a given 3D Mohr circle, four combinations of elements with different normal stress (σ) and shear stress (τ) are shown in Fig. 8. The σ_1, σ_2 and σ_3 are principal stresses loaded on the planes of the element with $\sigma_1>\sigma_2>\sigma_3$. In Fig. 8e, the inclined section is not parallel to any axis, and n is exterior normal to the inclined section. In the inclined section, the normal stress and shear stress are defined as σ_n and τ_n:

$$\sigma_n=\sigma_1\cos^2\alpha+\sigma_2\cos^2\beta+\sigma_3\cos^2\gamma \quad (2)$$

$$\tau_n=\sqrt{\sigma_1^2\cos^2\alpha+\sigma_2^2\cos^2\beta+\sigma_3^2\cos\gamma-\sigma_n^2} \quad (3)$$

where α is the angle between exterior normal, n, and x-axis, β is the angle between exterior normal, n, and y-axis, γ is the angle between exterior normal, n, and z-axis. The values of σ_n and τ_n are equal to the values of σ and τ in K area (K area including the edges stands for the stress range of σ_n and τ_n) (Fig. 8a and e).

The maximum principal stresses (σ_{max}) and maximum shear stresses (τ_{max}) were analyzed by using the stress-based fracture initiation criterion, which was developed by Bobet (1997) and revised by Silva and Einstein (2013, 2014). The criterion for tensile/compressive fracture initiation and propagation shows that the fracture will develop in a direction of θ, in which the tangential stress σ_θ (Fig. 9a) reaches the maximum ($\sigma_{\theta max}$) stress at the tip of the existing fracture:

$$\frac{\partial\sigma_\theta}{\partial\theta}=0 \quad \frac{\partial^2\sigma_\theta}{\partial\theta^2}>0 \quad (4)$$

When $\sigma_{\theta max}=\sigma_\theta^{crit}$, σ_θ^{crit} is the critical tangential stress.

For shear fracture initiation and followed propagation, the shear fracture will develop along the direction of θ, in which the shear stress τ_θ (Fig. 9a) reaches the maximum ($\tau_{\theta max}$) stress at the tip of the existing fracture:

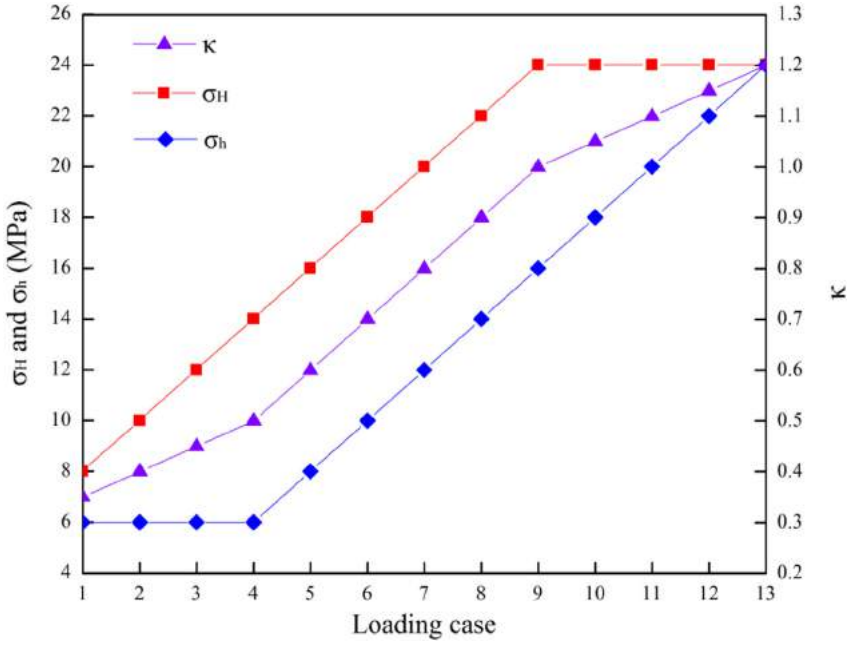

Fig. 7. Loading scenarios considered in the analysis of single-fracture model. The stress conditions were classified as three groups, i.e. case 1–4, case 5–9, and case 10-13.

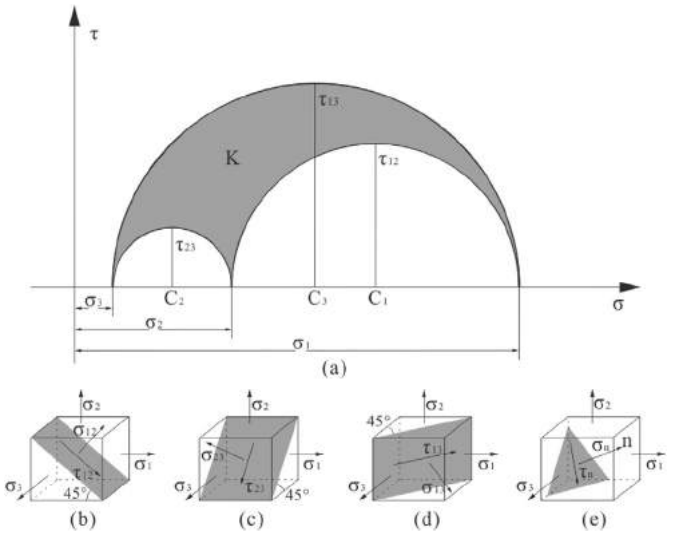

Fig. 8. The 3D Mohr circle and stress state of four elements. (a) Schematic diagram of 3D Mohr circle; Circle-C_1, Circle-C_2 and Circle-C_3 represent three special stress states of element-b, element-c and element-d, respectively; (b) the element-b, the range of σ and τ are $\sigma_2 \le \sigma \le \sigma_1$ and $0 \le \tau \le (\sigma_1-\sigma_2)/2$; (c) element-c, the range of σ and τ are $\sigma_3 \le \sigma \le \sigma_2$ and $0 \le \tau \le (\sigma_2-\sigma_3)/2$; (d) element-d, the range of σ and τ are $\sigma_3 \le \sigma \le \sigma_1$ and $0 \le \tau \le (\sigma_1-\sigma_3)/2$; (e) element-e represents a normal *in-situ* stresses condition, the section is not parallel to any principal plane.

$$\frac{\partial \tau_\theta}{\partial \theta} = 0 \quad \frac{\partial^2 \tau_\theta}{\partial \theta^2} < 0 \tag{5}$$

If $\tau_{\theta max} = \tau_\theta^{crit}$, τ_θ^{crit} is the critical shear stress.

However, the σ_{max} should be further divided into the principal tensile stress and compressive stress in the numerical simulation, which presents as positive value and negative value respectively. Tensile fracture will initiate at the location with the highest tensile stress, whereas the compressive fracture will initiate where the highest compressive stress is (here the minimum value was selected for the highest compressive stress due to the negative given value for compressive stress in ANSYS workbench). The fracture initiation type relates to the size of mechanical strength and the magnitudes of the tensile, compressive and shear stress (Silva and Einstein, 2013, 2014), which indicates that if the mechanical stress of the rock is broke through by tensile stress, then tensile fracture will develop. Similarly, compressive fracture develops when the rock is made breakthrough by compressive stress, which is same for the shear fractures.

3. Results

3.1. Modeling results

The magnitudes of σ_{max} and τ_{max} along the path for the 13 suits of loading scenarios are presented in Figs. 10 and 11. The σ_{max} magnitude along the stress path ranges from −15 to −2.5 MPa (Fig. 10a, b & c), the τ_{max} magnitude varies from 0.5 to 7.2 MPa (Fig. 11a, b & c). The σ_{max} is compressive stress along the path and it is negative. The results show that the σ_{max} increases as κ increase from 0.35 to 0.50, with growing horizontal stress difference (Figs. 7 and 10a), whereas it decreases as κ increase from 0.60 to 1.00, with a constant horizontal stress difference (Figs. 7 and 10b). In contrast, the horizontal stress difference decreases with κ increases from 1.05 to 1.20 (Fig. 7), the σ_{max} emerges a large fluctuation trend along the stress path (Fig. 10c), which can be seen that the σ_{max} changes drastically when κ increases from 1.0 to 1.05. In other words, the increase of σ_h with a constant σ_H can lead to the change of σ_{max}. The lowest of σ_{max} (approximately of −15 MPa for $\kappa = 1.05$) is obtained at $\theta = 42^\circ$ (Fig. 10c), which means that there is the highest potential to initiate the compressive fracture at $\theta = 42^\circ$.

The variations of τ_{max} along the path for 13 loading scenarios are presented in Fig. 11. For cases 1–4 as shown in Fig. 11a, the highest τ_{max} is approximately of 7.30 MPa at $\theta = 10^\circ$ or 70°, which means that the shear fracture initiation possibly occurs at $\theta = 10^\circ$ or 70°. For cases 5–9, shear fracture possibly occurs at $\theta = 45^\circ$ when the τ_{max} obtains the highest value of ~6.1 MPa (Fig. 11b). For cases 10–13, the τ_{max} emerges a decrease trend followed by the increasing of κ when θ between -90° and -30°, the highest τ_{max} (approximately of 3.0 MPa for $\kappa = 1.05$) is obtained at $\theta = -75^\circ$ (Fig. 11c).

3.2. Experimental results

Hydraulic fractures in coal blocks 1# and 2# created under the tri-axial conditions are presented in Fig. 12. The results show that horizontal and inclined fractures are generally distributed in coal block 1#, while the vertical fractures well developed in coal block 2#. Detailed parameters of the hydraulic fractures are displayed in Table 2.

For a local region in Fig. 12a, the section is parallel to the direction of σ_H, which shows that the original fractures scarcely developed in coal block 1#. The fracturing fluids were mainly injected into the coal block from the bottom of the simulated wellbore because of the vertical well fracturing. As shown in Fig. 12a, the yellow tracer in fracturing fluid can help to observe the original and induced fractures in coals. Many inclined fractures (IF)

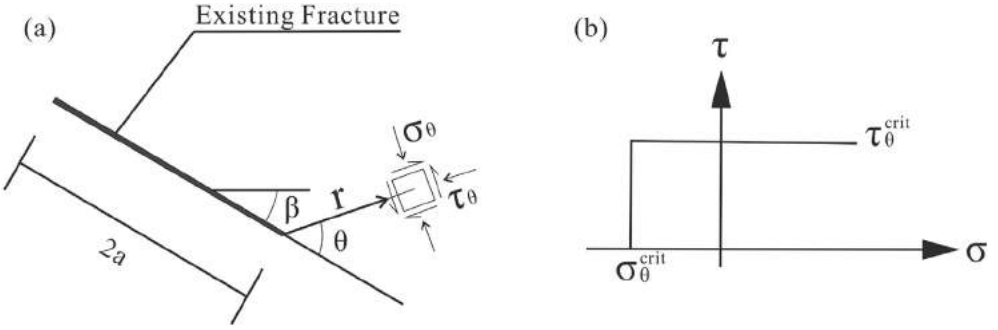

Fig. 9. (a) Stress field around a fracture tip, showing the cylindrical stresses of an element radial to the fracture tip (b) illustration of Bobet's stress-based criterion (Bobet, 1997).

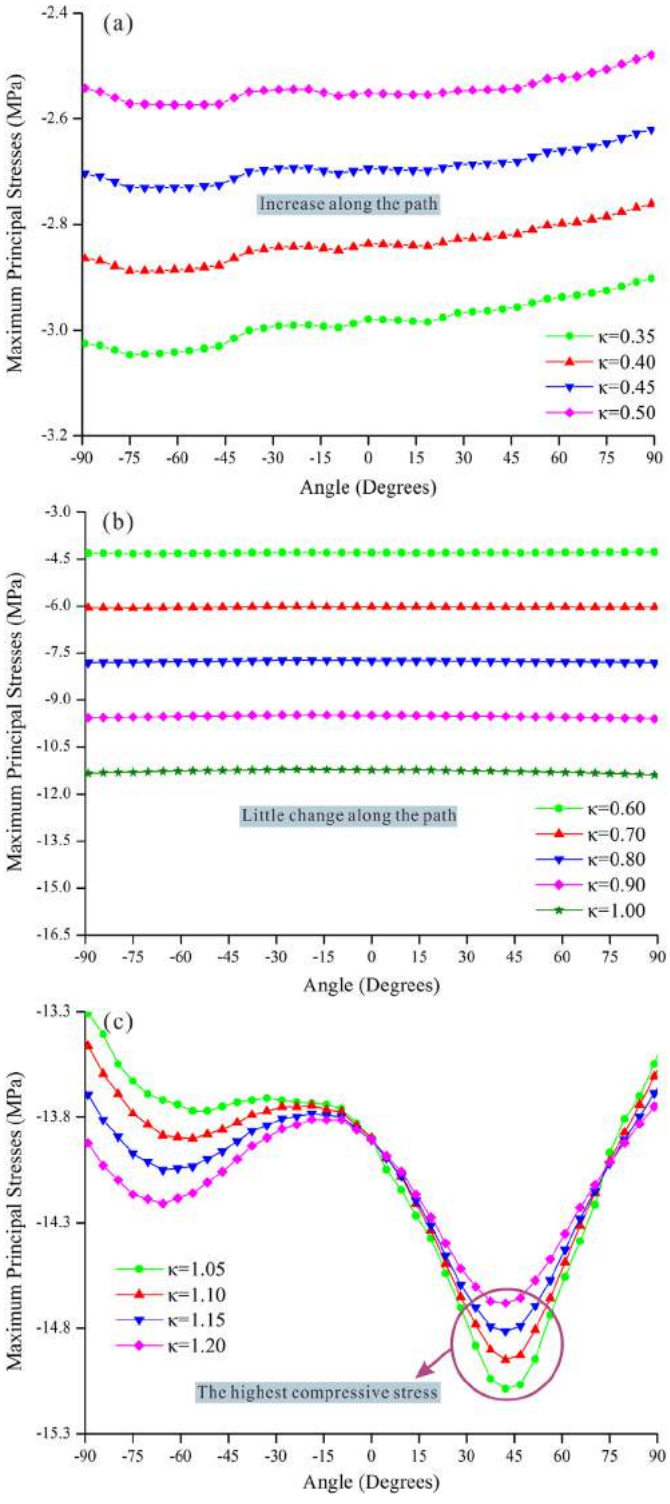

Fig. 10. Variation of σ_{max} along the path. The values of κ in loading scenarios 1–4 (a), loading scenarios 5–9 (b) and loading scenarios 10–13 (c) were low, medium and high, respectively.

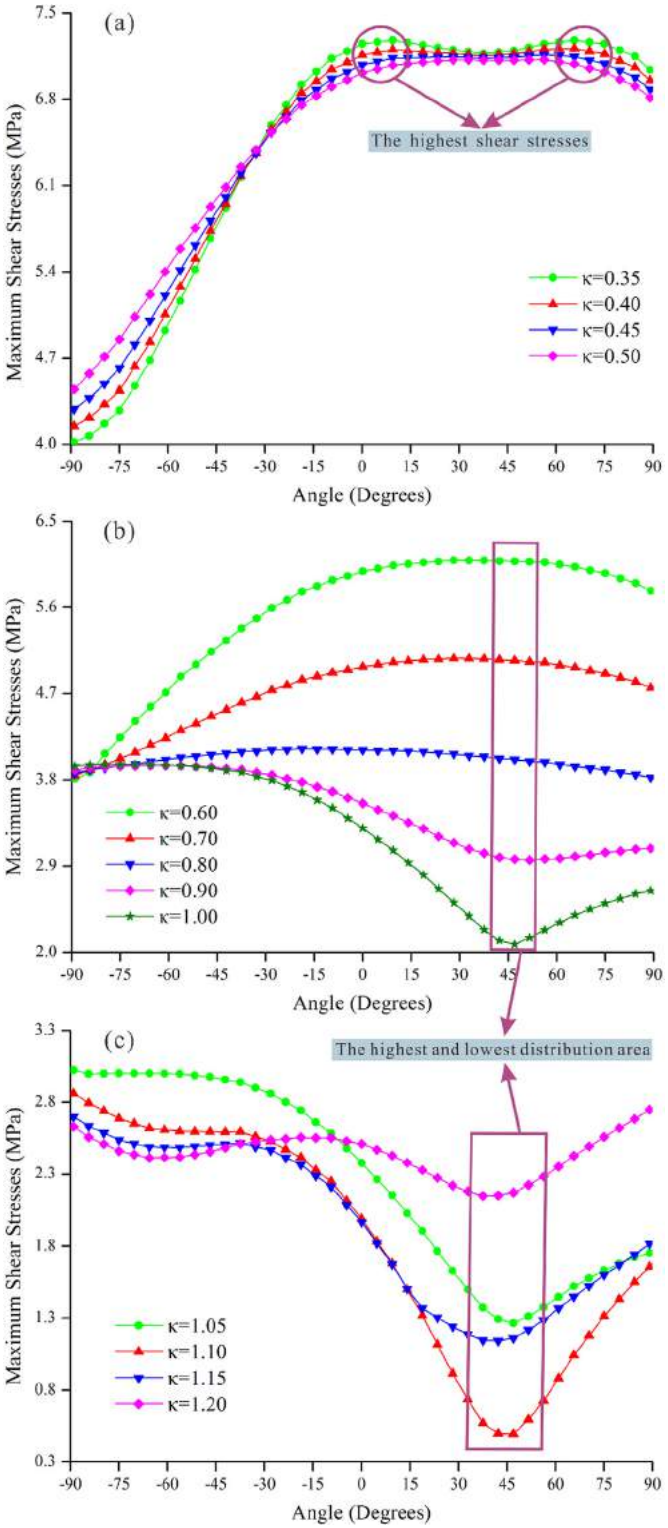

Fig. 11. Variation of τ_{max} along the path. The values of κ in loading scenarios 1–4(a), loading scenarios 5–9(b) and loading scenarios 10–13(c) were low, medium and high, respectively.

were created in the section of coal block 1#, the length, width and fracture density are 1–3 cm, 0.01–0.1 cm and 3/100 cm^2, respectively. And the created fractures are mostly initiated by fracturing fluids in the longitudinal. Fracturing fluids also appeared in natural fractures (NF), which are the main channels for the fracturing fluids migration. Some small fractures that close to a natural fracture are produced with the approaching angle of 30° as displayed in Fig. 12b, which indicates that the natural fracture initiates at the left tip, the horizontal fracture propagates along the direction of σ_H, and the inclined fracture is created around the left tip. Also, some relatively large fractures are showed on the surface of coal block 1# (Fig. 12c),

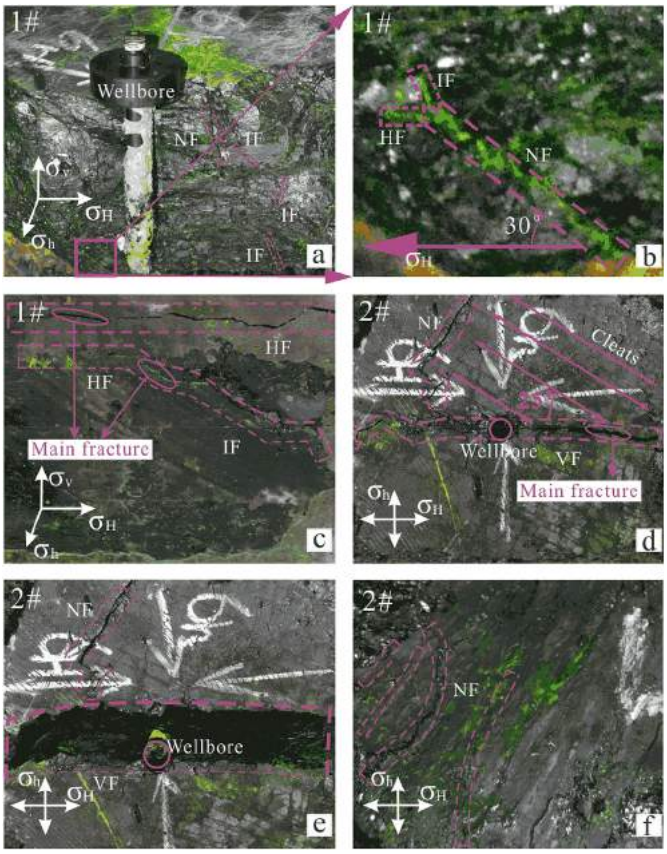

Fig. 12. The coal block and fractures after hydraulic fracturing experiment. (a) A vertical section of the coal block after hydraulic fracturing, (b) a natural fracture was cracked during hydraulic fracturing, the approaching angle is 30° for this fracture, (c) one side of the coal block, one major horizontal fracture and an inclined fracture were generated. (d) (e) A major vertical fracture was generated along the direction of σ_H, (f) natural fractures were developed in local coal block. HF is horizontal fracture; NF is natural fracture; IF is inclined fracture; VF is vertical fracture.

one fracture propagates along the horizontal direction, while another fracture propagates along the horizontal direction at the beginning, and then changes to the inclined direction. This interest phenomenon has been reported previously (Warpinski and Teufel, 1984), which indicates that the geologic discontinuities, such as joints, faults, and bedding planes, in conjunction with the deviatoric *in-situ stress* state, material properties, and permeability have significant impact on the overall geometry of hydraulic fractures. And there are almost no fracturing fluids that escape from the coal block.

For coal block 2#, one main vertical fracture is created near the wellbore, and one natural fracture is perpendicular to the cleats (Fig. 12d and e). The cleats are not cracked by fracturing fluids, and the new-created fracture cross the cleats at a certain angle of ~25°, which implies that the cleats are not the preferential propagation channel for fracturing. Furthermore, many natural fractures are also presented on the surface of the coal block #2 as coal block #1, which become the seepage channels for fracturing fluids. The fracturing fluids were founded on the block surface, which should be due to the leak of fracturing fluids. And the leak of fracturing fluids may lead to the decrease of hydraulic pressure; therefore the leak of fracturing fluids has a negative effect on fracturing (Fig. 12f).

4. Discussion

4.1. Effect of lateral stress coefficient (κ) on fracture initiate point

In order to investigate how the fracture initiation point changes with the increases of κ, the magnitude of highest σ_{max} and τ_{max} for 13 loading scenarios are plotted against the fracture initiation angle (θ) and κ (see Fig. 13). The σ_{max} decreases from −1.75 MPa to −14.90 MPa as κ increases from 0.35 to 1.20, which means that a higher κ can lead to a higher magnitude of principal compressive stress. Thus, the high lateral stress coefficient is favorable for the generation of a new compressive fracture (Fig. 13a). The results clearly show that fracture initiation angles can be divided into three phases, as shown in Fig. 13a. For κ in the range of 0.35–0.70, $\sigma_v>\sigma_H>\sigma_h$, the fracture initiation angle remains constant at a value of $\theta = 75°$. The θ changes suddenly when $\sigma_H = \sigma_v$, and the fracture initiation angles are approximately $\theta = 90°$ as κ increases from 0.80 to 1.05. Whereas, the θ changes approximately to 42° when $\sigma_h = \sigma_v$, and the θ remains at the same value for κ increases from 1.10 to 1.20. The τ_{max} decreases from 7.28 MPa to 2.58 MPa as κ varies from 0.35 to 1.20. Similarly, the shear fracture initiation angles emerge a same trend with the τ_{max} (Fig. 13b), which means that a higher κ leads to a lower τ_{max}. Therefore high lateral stress coefficient is not conducive to shear fracture. Tunsakul et al. (2013) also confirmed that lateral stress coefficient has a strong influence on the position of fracture initiation and the direction of the fracture propagation. The angle of compressive fracture initiation steeply shifts when $\sigma_H = \sigma_v$ or $\sigma_h = \sigma_v$ (Fig. 13a). In contrast, when $\sigma_H = \sigma_v$ or $\sigma_h = \sigma_v$, there is no significant changes on shear fracture (Fig. 13b). Four stress nephograms are selected to show the variations of the σ_{max} and τ_{max} (Fig. 14). The circles that focused on the fracture tip stand for the area of fracture initiation.

4.2. Fracture models related to stress orientation

2D cross section of stress vectors are presented in Fig. 15. The σ_H, σ_v and σ_h are parallel to the orientation of the x-axis, y-axis and z-axis, respectively. The vertical fracture initiated when the newly-created fracture propagates along y-axis. Similarly, the horizontal fracture initiated if the newly-created fracture propagates on the x-z plane (the z-axis is out-of-plane). Hubbert and Willis (1957) claimed that fractures commonly propagate along the orientation of σ_{max}. Recently, the numerical simulation conducted by Zhou et al. (2016) illustrated that a fracture will follow the direction of the *in-situ* σ_{max} when the hydraulic pressure is less than the maximum stress. Therefore, the orientation of σ_{max} is an important factor for predicting the fracture propagation direction.

As shown in Fig. 15(a–f), for κ of 0.35–0.70 and $\sigma_v>\sigma_H>\sigma_h$, the directions of minimum principal stress (σ_{min}), intermediate

Table 2
Parameters of the main hydraulic fracture by fracturing.

Coal block	Main fracture				
	Quantity	Length (cm)	Width (cm)	Direction	Type
1#	1	28	0.03–0.30	Parallel to the σ_H	Horizontal
1#	1	32	0.01–0.03	Oblique to the σ_H	Inclined
2#	1	35	0.10–0.50	Parallel to the σ_H	Vertical

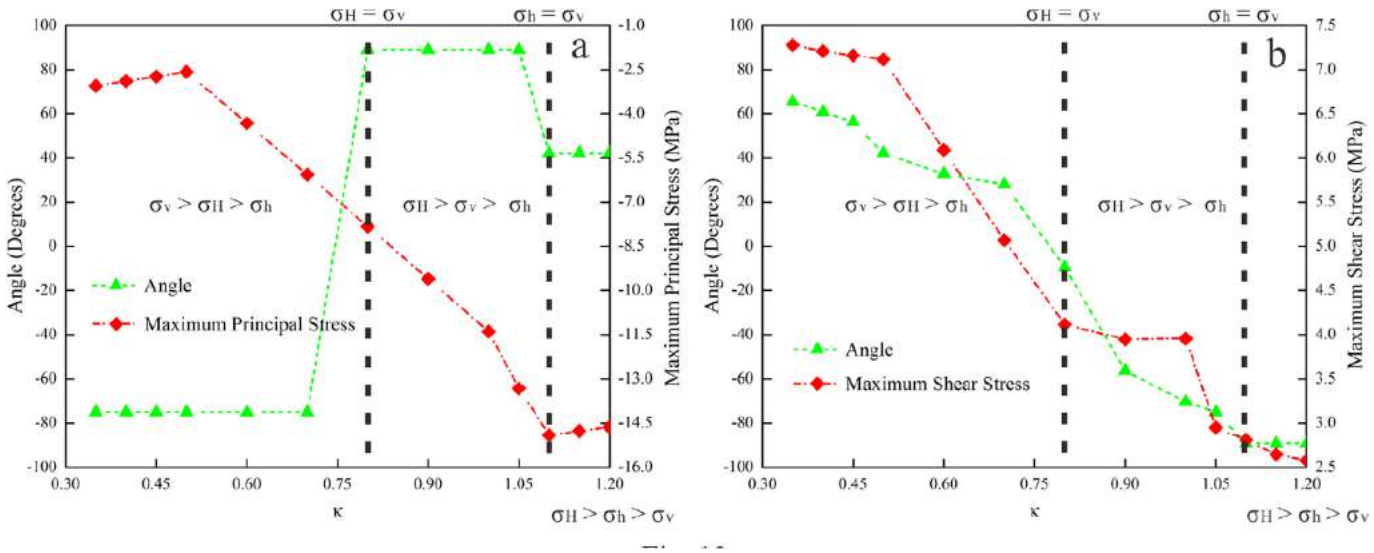

Fig. 13. Relationships of (a) maximal compressive σ_{max} vs. fracture initiation angle (θ), and (b) maximal τ_{max} vs. θ, with respect to different κ.

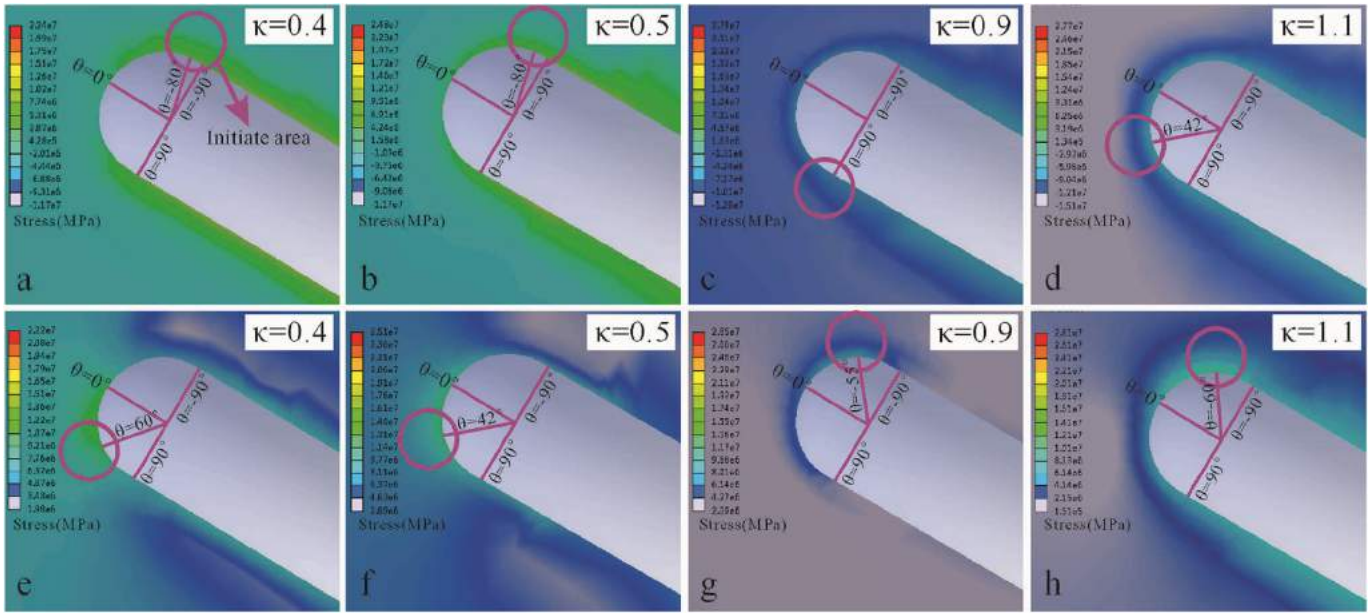

Fig. 14. Displays the maximum principal stresses around the fracture tip (a) (b) (c) and (d); the maximum shear stresses around the fracture tip (e) (f) (g) and (h).

principal stress (σ_{mid}) and σ_{max} are parallel to y-axis, x-axis and z-axis, respectively. Thus, the newly-created fracture can propagate along the z-axis at the x-z plane, and lead to a horizontal fracture. For $\kappa = 0.80$, $\sigma_v = \sigma_H > \sigma_h$, the directions of σ_{max} and σ_{min} are parallel to z-axis and the boundaries of natural fracture (Fig. 15g), the complex stress conditions can produce a variety of fracture types in this case.

For κ of 0.90–1.05 and $\sigma_H > \sigma_v > \sigma_h$, the directions of σ_{min}, σ_{mid} and σ_{max} are parallel to x-axis, y-axis and z-axis respectively (Fig. 15h, i & j), which means that the newly-created fracture propagate along the z-axis and at the y-z plane. Thus, a vertical fracture is occurs under this condition.

For $\kappa = 1.10$ and 1.15, corresponding to $\sigma_H > \sigma_h = \sigma_v$ and $\sigma_H > \sigma_h > \sigma_v$, the directions of σ_{min}, σ_{max} and σ_{mid} near the natural fracture are parallel to x-axis, y-axis and z-axis, respectively (Fig. 15k and l). Similarly to κ of 0.90–1.05, vertical fracture is presents.

For $\kappa = 1.20$, $\sigma_H = \sigma_h > \sigma_v$, the directions of σ_{min}, σ_{max} and σ_{mid} are parallel to z-axis, y-axis and x-axis near the fracture, respectively (Fig. 15m), thus, a vertical fracture is created.

4.3. Relation between fracture propagation and σ_H orientation

The hydraulic fracture propagation follows the least resistance path (Liu et al., 2014). Based on the fracturing experiments, the newly-created fractures frequently change their propagation orientations (Fig. 12(a–f)), which illustrates that the mechanics of coal heterogeneity should be one of the reasons that results in uneven of fracture propagation. The main horizontal fracture in Fig. 12c and the vertical fracture in Fig. 12d are approximately consistent with the direction of σ_H, while the natural fracture in Fig. 12e is oblique to σ_H. Previous results by Hickman et al. (1985) also agreed that the azimuths of σ_H are determined from the orientations of hydraulic fractures that are then averaged to obtain the average direction of

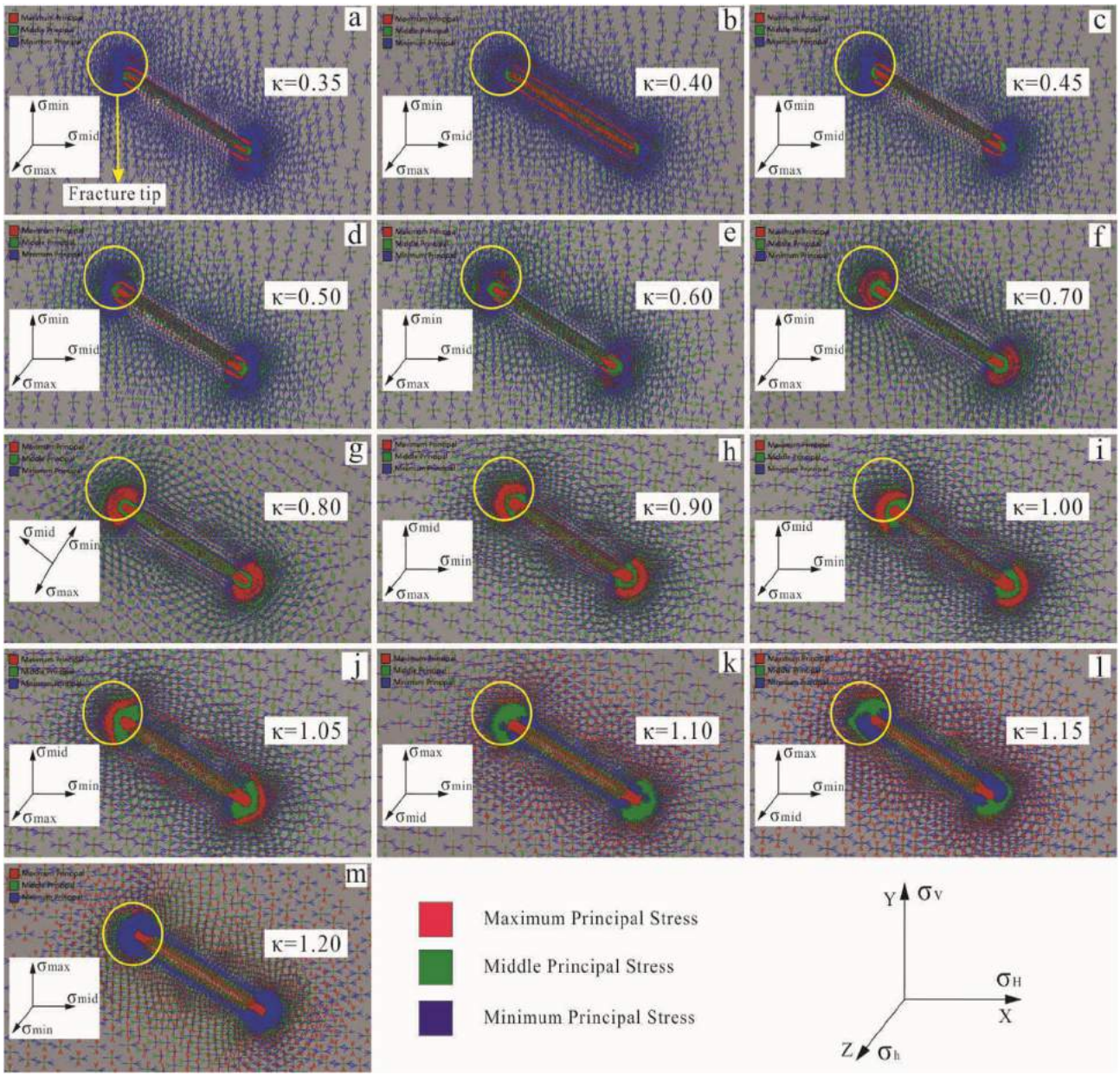

Fig. 15. Stress vectors of 13 loading scenarios plot in Fig. 15(a–m). The red, green, and blue point the directions of σ_{max}, σ_{mid} and σ_{min}, respectively. The natural fracture is surrounded by the yellow line; the coordinates in Fig. 15(a–m) represent the directions of σ_{max}, σ_{mid} and σ_{min} around the fracture tip. (For interpretation of the references to colour in this figure legend, the reader is referred to the web version of this article.)

σ_H. Moreover, the fractures were classified into two systems by Ameen (2014): a younger major system is nearly parallel to the current σ_H and perpendicular to σ_h, therefore the younger major fracture system should enhance reservoir permeability and an older, minor, fully mineralized system is not conducive to improve the reservoir permeability. In this study, the initiate directions of hydraulic fractures from the experiment are consistent with the direction of σ_H as shown in Fig. 12c and d, which illustrates that the fracture distribution can be used to evaluate the distribution of *in-situ* stresses.

4.4. Effect of horizontal stress difference on fracture type

Horizontal stress difference has a great influence on the hydraulic fracture initiation (Blanton, 1986; Zhou et al., 2008; Liu et al., 2014). In this hydro-fracturing experiment, the value of κ is 0.81 for coal block 1#, which is similar with the loading case 7. Consistent with coal block 1#, the horizontal stress difference are 6 MPa for both loadings case 3 and 10, while the κ varies. The simulation results of loading case 7 agree well with the experimental results, of which both horizontal and inclined fractures are developed (Fig. 12a and b). The prediction results for loading case 3 and 10 are horizontal and vertical fractures, respectively (Fig. 15c and j). Similarly, for coal block 2# and loading case 9, $\kappa = 1.01$, and the simulation results of loading case 9 indicate a vertical fracture should be created, which agrees well with coal block 2# that one main vertical fracture is created (Fig. 12d). Furthermore, the horizontal stress differences of coal block 2# ($\kappa = 1.01$), loading case 2 ($\kappa = 0.4$) and 11 ($\kappa = 1.1$) are 4 MPa. Although the κ of loading case 11 is close to coal block 2#, the simulation results show that only

loading case 11 can create vertical fracture (Fig. 15b and k). Recently, Liu et al. (2014) also demonstrated that horizontal differential stress should be one of the dominating factors of hydraulic fractures initiation and propagation. According to the above discussions, a close value of κ should cause the same fracture types, whereas the same horizontal differential stress with different κ should lead to different fracture types. It can be concluded that, the horizontal stress difference has less impact on the fracture type, under the same σ_v applied. However, the value of κ determines the fracture type, which is consistent with the previous experimental results (Tunsakul et al., 2013).

The value of hydraulic pressure applied to the model is relatively low (6 MPa). Therefore σ_{max} approximately is compressive stress in this study. A higher value of hydraulic pressure may arouse excessive mechanical failure in part of the model. The approaching angle used is 30°, which also affect the stress distribution around the natural fracture (Guo et al., 2015). Although the impact of lateral stress coefficient on fracture initiation with employing a single-fracture model has been well discussed, further works for multi-fractures model and the coals with different mechanical properties should be introduced to evaluate their impacts on the fracture initiation and propagation.

5. Conclusion

The initiation mechanisms of natural fractures during hydraulic fracturing in Zhengzhuang coals from the SQB, north China are discussed both with the numerical simulations and experiments. The results obtained from this work could be applied in the field work, such as prediction of the newly-created fracture initiation type, propagation direction during hydraulic fracturing and evaluation of the reservoir permeability after fracturing. The detailed conclusions may include:

1) The highest compressive stress increases and shear stress decreases with increasing the lateral stress coefficient (κ); this demonstrates that a higher κ is not conducive to create shear fracture but favorable to form a new compressive fracture. $\sigma_H = \sigma_v$ or $\sigma_h = \sigma_v$ has a great influence on the initiate location of the compressive fracture, whereas it has no significant influence on shear fracture.
2) With the same σ_v applied, the horizontal stress difference has little impact on the type of newly-created fracture, and the value of κ determines the type of the fracture.
3) The lateral stress coefficient plays a critical role in determining the stress magnitude and orientation around the fracture tip. Horizontal fracture is the main type when $\sigma_v > \sigma_H > \sigma_h$, whereas the vertical fracture possibly occur when $\sigma_H > \sigma_v > \sigma_h$. There is a high probability for developing inclined fractures in the coals with strong heterogeneity.

Acknowledgements

This research was funded by the National Natural Science Foundation of China (grant no. 41602170), the Fundamental Research Funds for Central Universities (grant no. 35832015136) and Key Project of Coal-based Science and Technology in Shanxi Province-CBM accumulation model and reservoir evaluation in Shanxi province (grant no. MQ2014-01).

References

Ameen, M.S., 2014. Fracture and *in-situ* stress patterns and impact on performance in the Khuff structural prospects, eastern offshore Saudi Arabia. Mar. Pet.. Geol. 50, 166–184.
Barr, S.P., Hunt, D.P., 1999. Anelastic strain recovery and the Kaiser effect retention span in the Carnmenellis granite, UK. Rock Mech. Rock Eng. 32, 169–193.
Beekman, F., Badsi, M., Wees, J.D.V., 2000. Faulting, fracturing and in situ stress prediction in the Ahnet Basin, Algeria - a finite element approach. Tectonophysics 320, 311–329.
Blanton, T.L., 1986. Propagation of hydraulically and dynamically induced fractures in naturally fractured reservoirs. Proceedings of the SPE/DOE symposium on unconventional gas, Louisville, Kentucky, SPE Paper 15261.
Bobet, A., 1997. Fracture Coalescence in Rock Materials: Experimental Observations and Numerical Predictions. Sc.D. Thesis. Massachusetts Institute of Technology, Cambridge, MA, USA.
Bohloli, B., Pater, C.J.D., 2006. Experimental study on hydraulic fracturing of soft rocks: influence of fluid rheology and confining stress. J. Pet. Technol. 53, 1–12.
Brown, E.T., Hoek, E., 1978. Trends in relationships between measured *in-situ* stresses and depth. Int. J. Rock Mech. Min. Geomech. Abstr. 15, 211–215.
Brudy, M., Zoback, M.D., 1999. Drilling-induced tensile wall-fractures: implications for determination of *in-situ* stress orientation and magnitude. Int. J. Rock Mech. Min. 36, 191–215.
Cai, Y., Liu, D., Yao, Y., et al., 2011. Geological controls on prediction of coalbed methane of No. 3 coal seam in Southern Qinshui Basin, North China. Int. J. Coal Geol. 88, 101–112.
Charlez, P., Despax, D., 1985. The state of stress in the earth crust: its importance in petroleum engineering. 14th Annual Convention Proceedings, Indonesian Petroleum Association. 2, 299–308.
Chatterjee, R., 2008. Effect of normal faulting on *in-situ* stress: a case study from Mandapeta Field, Krishna-Godavari basin, India. Earth Planet. Sc. Lett. 269, 458–467.
Cleary, M.P., Wong, S.K., 1985. Numerical simulation of unsteady fluid flow and propagation of a circular hydraulic fracture. Int. J. Numer. Anal. Met. 9, 1–14.
Filimonov, Y.L., Lavrov, A.V., Shafarenko, Y.M., Shkuratnik, V.L., 2001. Memory effects in rock salt under triaxial stress state and their use for stress measurement in a rock mass. Rock Mech. Rock Eng. 34, 275–291.
Gordeliy, E., Peirce, A., 2013. Coupling schemes for modeling hydraulic fracture propagation using the XFEM. Comput. Method. Appl. M. 253, 305–322.
Guo, T.K., Zhang, S.C., Qu, Z.Q., Zhou, T., Xiao, Y.S., Gao, J., 2014. Experimental study of hydraulic fracturing for shale by stimulated reservoir volume. Fuel 128, 373–380.
Guo, T.K., Zhang, S.C., Zou, Y.S., Xiao, B., 2015. Numerical simulation of hydraulic fracture propagation in shale gas reservoir. J. Nat. Gas. Sci. Eng. 26, 847–856.
Heffer, K.J., Koutsabeloulis, N.C., 1995. Stress Effects on Reservoir Flow: Numerical Modeling Used to Reproduce Field Data, vol. 84. Geological Society, Special Publications, London, pp. 81–88.
Hickman, S.H., Healy, J.H., Zoback, M.D., 1985. In Situ stress, natural fracture distribution, and borehole elongation in the Auburn geothermal well, Auburn, New York. J. Geophys. Res. Atmos. 90, 5497–5512.
Hillis, R.R., 1998. The influence of fracture stiffness and the in situ stress field on the closure of natural fractures. Pet.. Geosci. 4, 57–65.
Hoek, E., Brown, E.T., 1980. Underground excavation in rock. Inst. Min. Metall., London.
Huang, B., Li, P., Ma, J., et al., 2013. Experimental investigation on the basic law of hydraulic fracturing after water pressure control blasting. Rock Mech. Rock Eng. 47, 1321–1334.
Hubbert, M.K., Willis, D.G., 1957. Mechanics of hydraulic fracturing. J. Pet.. Technol. 9, 153–168.
Jaeger, J.C., Cook, N.G.W., 1979. Science Paperbacks. Fundamentals of rock mechanics, third ed., 9, pp. 251–252
Jeffrey, R., Bunger, A., Jeffrey, R., 2009. A detailed comparison of experimental and numerical data on hydraulic fracture height growth through stress contrasts. SPE J. 14, 413–422.
Kaiser, J., 1953. Erkenntnisse und Folgerungen aus der Messung von Geräuschen bei Zugbeanspruchung von metallischen Werkstoffen. Arch. Fr. Das. Eisenhttenwes. 24, 43–45.
Karacan, C.Ö., Okandan, E., 2000. Fracture/cleat analysis of coals from Zonguldak Basin (northwestern Turkey) relative to the potential of coalbed methane production. Int. J. Coal Geol. 44, 109–125.
Kim, J., Moridis, G.J., 2015. Numerical analysis of fracture propagation during hydraulic fracturing operations in shale gas systems. Int. J. Rock Mech. Min. 76, 127–137.
Laubach, S.E., Olson, J.E., Gale, J.F.W., 2004. Are open fractures necessarily aligned with maximum horizontal stress? Earth Planet. Sc. Lett. 222, 191–195.
Lavrov, A., 2001. Kaiser effect observation in brittle rock cyclically loaded with different loading rates. Mech. Mater 33, 669–677.
Lehtonen, A., Cosgrove, J.W., Hudson, J.A., et al., 2012. An examination of in situ rock stress estimation using the Kaiser effect. Eng. Geol. 124, 24–37.
Li, C., Nordlund, E., 1993. Experimental verification of the Kaiser effect in rocks. Rock Mech. Rock Eng. 26, 333–351.
Li, H., Wong, L.N.Y., 2012. Influence of flaw inclination angle and loading condition on crack initiation and propagation. Int. J. Solids Struct. 49, 2482–2499.
Li, Q., Lin, B., Zhai, C., 2014. The effect of pulse frequency on the fracture extension during hydraulic fracturing. J. Nat. Gas. Sci. Eng. 21, 296–303.
Liu, G.H., Pang, F., Chen, Z.X., 2000. The principle of similarity criterion in the simulation experiment during hydraulic fracturing. J. China Univ. Pet. 24, 46–48.
Liu, Z., Chen, M., Zhang, G., 2014. Analysis of the influence of a natural fracture network on hydraulic fracture propagation in carbonate formations. Rock Mech.

Rock Eng. 47, 575–587.
Majdi, A., Hassani, F.P., Nasiri, M.Y., 2012. Prediction of the height of destressed zone above the mined panel roof in longwall coal mining. Int. J. Coal Geol. 98, 62–72.
Mcclure, M.W., Babazadeh, M., Shiozawa, S., Huang, J., 2016. Fully coupled hydro-mechanical simulation of hydraulic fracturing in 3D discrete-fracture networks. SPE J. 21, 1302–1320.
Meng, Z., Zhang, J., Wang, R., 2011. *In-situ* stress, pore pressure and stress-dependent permeability in the Southern Qinshui Basin. Int. J. Rock Mech. Min. Sci. 48, 122–131.
Moes, N., Dolbow, J., Belytschko, T., 1999. A finite element method for crack growth without remesing. Int. J. Numer. Meth. Eng. 46, 131–150.
Nelson, E.J., 2005. Transverse drilling-induced tensile fractures in the West Tuna area, Gippsland Basin, Australia: implications for the in situ stress regime. Int. J. Rock Mech. Min. Sci. 42, 361–371.
Paluszny, A., Zimmerman, R.W., 2011. Numerical simulation of multiple 3D fracture propagation using arbitrary meshes. Comput. Method Appl. Mech. Eng. 200, 953–966.
Paul, S., Chatterjee, R., 2011. Mapping of cleats and fractures as an indicator of *in-situ* stress orientation, Jharia Coalfield, India. Int. J. Coal Geol. 88, 113–122.
Philip, Z., Jennings, J., Olson, J., Laubach, S., Holder, J., 2005. Modeling coupled fracture-matrix fluid flow in geomechanically simulated fracture networks. SPE Reserv. Eval. Eng. 8, 300–309.
Rahman, M.M., Rahman, S.S., 2013. Studies of hydraulic fracture-propagation behavior in presence of natural fractures: fully coupled fractured-reservoir modeling in poroelastic environments. Int. J. Geomech. 13, 809–826.
Rinne, M., Shen, B., Backers, T., 2013. Modelling fracture propagation and failure in a rock pillar under mechanical and thermal loadings. J. Rock Mech. Geotech. Eng. 5, 73–83.
Shimizu, H., Murata, S., Ishida, T., 2011. The distinct element analysis for hydraulic fracturing in hard rock considering fluid viscosity and particle size distribution. Int. J. Rock Mech. Min. Sci. 48, 712–727.
Silva, B.G.D., Einstein, H.H., 2013. Modeling of crack initiation, propagation and coalescence in rocks. Int. J. Fract. 182, 167–186.
Silva, B.G.D., Einstein, H.H., 2014. Finite element study of fracture initiation in flaws subject to internal fluid pressure and vertical stress. Int. J. Solids Struct. 51, 4122–4136.
Stoeckhert, F., Molenda, M., Brenne, S., et al., 2015. Fracture propagation in sandstone and slate - laboratory experiments, acoustic emissions and fracture mechanics. J. Rock Mech. Geotech. Eng. 7, 237–249.
Taleghani, A.D., Olson, J.E., 2011. Numerical modeling of multi-stranded-hydraulic-fracture propagation: accounting for the interaction between induced and natural fractures. SPE J. 16, 575–581.
Taleghani, A.D., Olson, J.E., 2014. How natural fractures could affect hydraulic-fracture geometry. SPE J. 19, 161–171.
Teng, J., Yao, Y., Liu, D., et al., 2015. Evaluation of coal texture distributions in the southern Qinshui Basin, North China: investigation by a multiple geophysical logging method. Int. J. Coal Geol. 140, 9–22.
Tunsakul, J., Jongpradist, P., Kongkitkul, W., et al., 2013. Investigation of failure behavior of continuous rock mass around cavern under high internal pressure. Tunn. Undergr. Sp. Tech. 34, 110–123.
Wang, T., Zhou, W., Chen, J., et al., 2014. Simulation of hydraulic fracturing using particle flow method and application in a coal mine. Int. J. Coal Geol. 121, 1–13.
Warpinski, N.R., Teufel, L.W., 1984. Influence of geologic discontinuities on hydraulic fracture propagation. J. Pet. Technol. U. S. 39, 209–220.
Wasantha, P.L.P., Konietzky, H., Weber, F., 2017. Geometric nature of hydraulic fracture propagation in naturally-fractured reservoirs. Comput. Geotech. 83, 209–220.
Yao, Y., 2012. Linear elastic and cohesive fracture analysis to model hydraulic fracture in brittle and ductile rocks. Rock Mech. Rock Eng. 45, 375–387.
Zhai, C., Yu, X., Xiang, X., et al., 2015. Experimental study of pulsating water pressure propagation in CBM reservoirs during pulse hydraulic fracturing. J. Nat. Gas. Sci. Eng. 25, 15–22.
Zhang, G.Q., Chen, M., 2010. Dynamic fracture propagation in hydraulic re-fracturing. J. Pet.. Sci. Eng. 70, 266–272.
Zhou, D., Zheng, P., He, P., et al., 2016. Hydraulic fracture propagation direction during volume fracturing in unconventional reservoirs. J. Pet.. Sci. Eng. 141, 82–89.
Zhou, J., Chen, M., Jin, Y., et al., 2008. Analysis of fracture propagation behavior and fracture geometry using a tri-axial fracturing system in naturally fractured reservoirs. Int. J. Rock Mech. Min. Sci. 45, 1143–1152.